ARTICLE

OPEN ACCESS

The faintest, extremely variable X-ray tidal disruption event from a supermassive black hole binary?

Mengqiu Huang,[1,2] Yongquan Xue,[1,2,*] Shuo Li,[3,*] Fukun Liu,[4,5] Shifu Zhu,[1,2] Jin-Hong Chen,[6] Rong-Feng Shen,[7,8] Yibo Wang,[1,2] Yi Yang,[9,10] Ning Jiang,[1,2] Franz Erik Bauer,[11,12,13] Cristian Vignali,[14,15] Fan Zou,[16] Jialai Wang,[1,2] Alexei V. Filippenko,[10] Bin Luo,[17,18] Chen Qin,[1,2] Jonathan Quirola-Vásquez,[19] Jun-Xian Wang,[1,2] Lulu Fan,[1,2] Mouyuan Sun,[20] Qingwen Wu,[21] Qingling Ni,[22] Thomas G. Brink,[10] Tinggui Wang,[1,2] Weikang Zheng,[10] Xinwen Shu,[23] Xuechen Zheng,[24] Xiaozhi Lin,[1,2] Xu Kong,[1,2] Yijun Wang,[17,18] Yibin Luo,[1,2] and Zheyu Lin[1,2]

*Correspondence: xuey@ustc.edu.cn (Y.X.); lishuo@nao.cas.cn (S.L.)

Received: July 14, 2025; Accepted: October 27, 2025; https://doi.org/10.1016/j.xinn.2025.101169

GRAPHICAL ABSTRACT

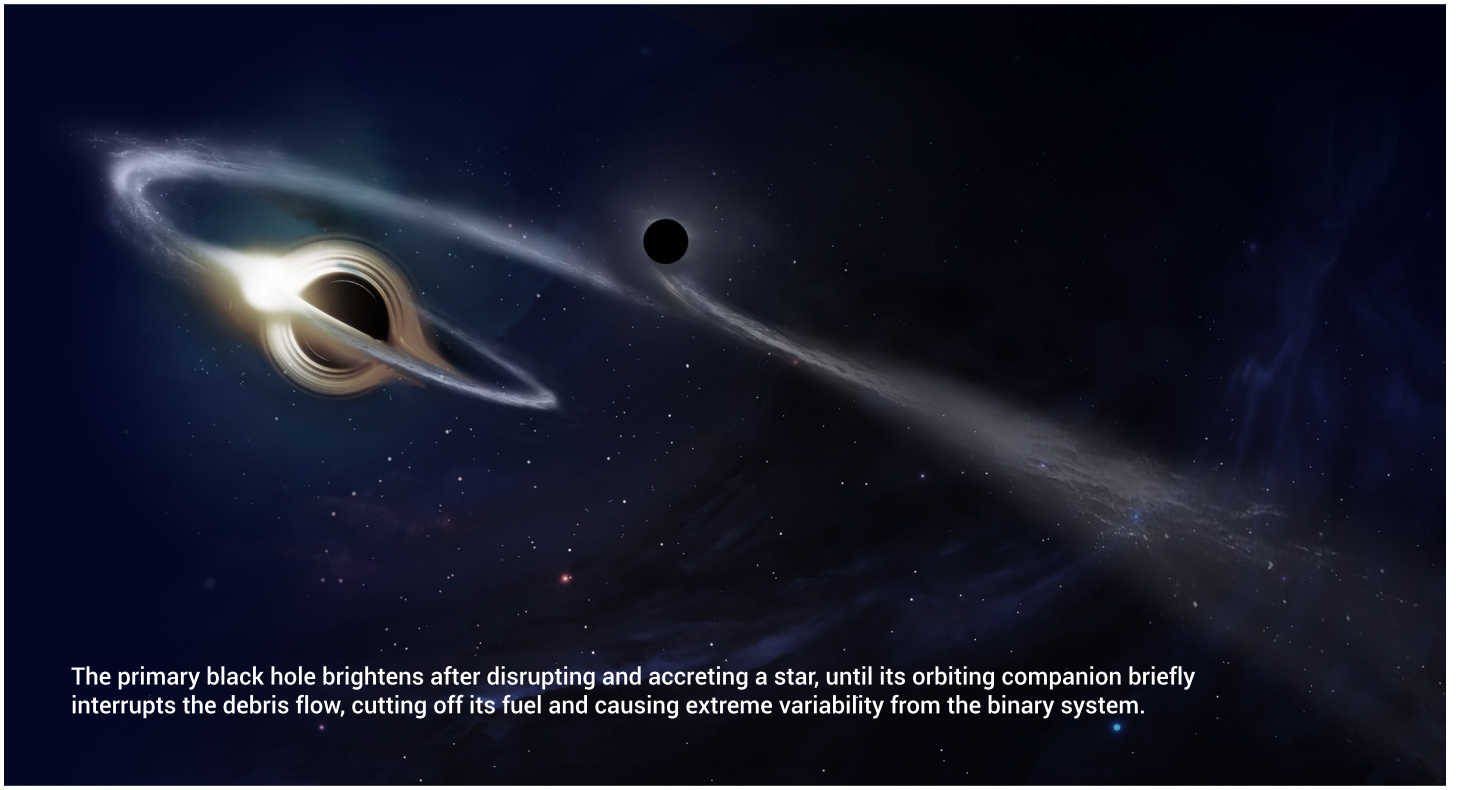

PUBLIC SUMMARY

- The source has the best X-ray coverage spanning ∼ 20 years with the deepest total exposure of ∼ 10 Ms.
- The source is the faintest X-ray-selected tidal disruption event (TDE) to date.
- The source displays unusually strong hard X-ray emission and extreme luminosity variability.
- The source is likely the most distant supermassive black hole binary TDE known to date.

OPEN ACCESS

ARTICLE

The Innovation

The faintest, extremely variable X-ray tidal disruption event from a supermassive black hole binary?

Mengqiu Huang,[1,2] Yongquan Xue,[1,2,*] Shuo Li,[3,*] Fukun Liu,[4,5] Shifu Zhu,[1,2] Jin-Hong Chen,[6] Rong-Feng Shen,[7,8] Yibo Wang,[1,2] Yi Yang,[9,10] Ning Jiang,[1,2] Franz Erik Bauer,[11,12,13] Cristian Vignali,[14,15] Fan Zou,[16] Jialai Wang,[1,2] Alexei V. Filippenko,[10] Bin Luo,[17,18] Chen Qin,[1,2] Jonathan Quirola-Vásquez,[19] Jun-Xian Wang,[1,2] Lulu Fan,[1,2] Mouyuan Sun,[20] Qingwen Wu,[21] Qingling Ni,[22] Thomas G. Brink,[10] Tinggui Wang,[1,2] Weikang Zheng,[10] Xinwen Shu,[23] Xuechen Zheng,[24] Xiaozhi Lin,[1,2] Xu Kong,[1,2] Yijun Wang,[17,18] Yibin Luo,[1,2] and Zheyu Lin[1,2]

[1]Department of Astronomy, University of Science and Technology of China, Hefei 230026, Anhui, China
[2]School of Astronomy and Space Science, University of Science and Technology of China, Hefei 230026, Anhui, China
[3]National Astronomical Observatories, Chinese Academy of Sciences, Beijing 100012, China
[4]Department of Astronomy, School of Physics, Peking University, Beijing 100871, China
[5]Kavli Institute for Astronomy and Astrophysics, Peking University, Beijing 100871, China
[6]Department of Physics, University of Hong Kong, Pokfulam Road, Hong Kong, China
[7]School of Physics and Astronomy, Sun Yat-sen University, Zhuhai 519082, China
[8]CSST Science Center for the Guangdong-Hong Kong-Macau Greater Bay Area, Sun Yat-sen University, Zhuhai 519082, China
[9]Department of Physics, Tsinghua University, Beijing 100084, China
[10]Department of Astronomy, University of California, Berkeley, Berkeley, CA 94720-3411, USA
[11]Instituto de Astrofísica, Facultad de Física and Centro de Astroingeniería, Pontificia Universidad Católica de Chile, Santiago 7820436 RM, Chile
[12]Millennium Institute of Astrophysics, Santiago 7500011 RM, Chile
[13]Space Science Institute, Boulder, CO 80301, USA
[14]Dipartimento di Fisica e Astronomia "Augusto Righi", Università degli Studi di Bologna, Via Gobetti 93/2, 40129 Bologna, Italy
[15]INAF – Osservatorio di Astrofisica e Scienza dello Spazio di Bologna, Via Gobetti 93/3, 40129 Bologna, Italy
[16]Department of Astronomy, University of Michigan, 1085 S University, Ann Arbor, MI 48109, USA
[17]School of Astronomy and Space Science, Nanjing University, Nanjing 210093, China
[18]Key Laboratory of Modern Astronomy and Astrophysics (Nanjing University), Ministry of Education, Nanjing 210093, China
[19]Department of Astrophysics/IMAPP, Radboud University Nijmegen, P.O. Box 9010, 6500 GL Nijmegen, the Netherlands
[20]Department of Astronomy, Xiamen University, Xiamen, Fujian 361005, China
[21]Department of Astronomy, School of Physics, Huazhong University of Science and Technology, Wuhan, Hubei 1037, China
[22]Max-Planck-Institut für extraterrestrische Physik (MPE), Gießenbachstraße 1, 85748 Garching bei München, Germany
[23]Department of Physics, Anhui Normal University, Wuhu, Anhui 241002, China
[24]Shanghai Astronomical Observatory, Chinese Academy of Sciences, Shanghai 200030, China
*Correspondence: xuey@ustc.edu.cn (Y.X.); lishuo@nao.cas.cn (S.L.)

Received: July 14, 2025; Accepted: October 27, 2025; https://doi.org/10.1016/j.xinn.2025.101169

Citation: Huang M., Xue Y., Li S., et al., (2026). The faintest, extremely variable X-ray tidal disruption event from a supermassive black hole binary? The Innovation **7(3)**, 101169.

Tidal disruption events (TDEs), which occur when stars enter the tidal radii of supermassive black holes (SMBHs) and are subsequently torn apart by their tidal forces, represent intriguing phenomena that stimulate growing research interest and pose an increasing number of puzzles in the era of time-domain astronomy. Here, we report an unusual X-ray transient, XID 935, discovered in the 7 Ms Chandra Deep Field-South, the deepest X-ray survey ever. XID 935 experienced an overall X-ray dimming by a factor of more than 40 between 1999 and 2016. Not monotonically decreasing during this period, its X-ray luminosity increased by a factor > 27 within 2 months, from $L_{0.5-7\,\mathrm{keV}} < 10^{40.87}$ erg s^{-1} (October 10, 2014–January 4, 2015) to $L_{0.5-7\,\mathrm{keV}} = 10^{42.31\pm0.20}$ erg s^{-1} (March 16, 2015). The X-ray position of XID 935 is located at the center of its host galaxy with a spectroscopic redshift of 0.251, whose optical spectra do not display emission characteristics associated with an active galactic nucleus. The peak 0.5–2.0 keV flux is the faintest among all the X-ray-selected TDE candidates to date. Thanks to a total exposure of ∼ 9.5 Ms in the X-ray bands, we manage to secure relatively well-sampled, 20-year-long X-ray light curves of this deepest X-ray-selected TDE candidate. We find that a partial TDE model could not explain the main declining trend. An SMBH binary TDE model is in acceptable accordance with the light curves of XID 935; however, it fails to match short-timescale fluctuations exactly. Therefore, the exceptional observational features of XID 935 provide a key benchmark for refining quantitative TDE models and simulations.

INTRODUCTION

In the early 1960s, the first quasi-stellar object (i.e., quasar) was discovered.[1] One possible power source of quasars was suggested[2] to be the tidal disruption of a star passing within the Roche limit of a supermassive black hole (SMBH), now known as a tidal disruption event (TDE). Later detailed research demonstrated that TDEs cannot release sufficient sustained energy to explain the persistent activity of an active galactic nucleus (AGN).[3,4] Nonetheless, an order of 10^6 stars are sacrificed over the lifetime of a galaxy,[5] so disrupted stars may not contribute significantly to the growth of an SMBH with a mass larger than $10^7\ M_\odot$, TDEs may affect the spin distribution for black holes with mass $\sim 10^6\ M_\odot$[6] and power observed AGNs in dwarf galaxies.[7] Although TDEs lost to Galactic-scale gas[5,8,9] in the race for providing fuel to AGNs, their unique characteristics are still an outstanding probe for revealing dormant SMBHs.[10] Since NGC 5905 was first noticed,[11] over 100 TDEs have been discovered, and probed with respectable amounts of multi-wavelength data. Recently, time-domain surveys[12,13] have propelled TDE research into a new era of proactive exploration, rather than relying on serendipitous discoveries in legacy data.

The TDE model described in Rees[10] neglects partial stellar disruptions, now known as the partial TDE (pTDE), in which the pericenter of the star is slightly farther from the tidal radius, resulting in a surviving stellar core after the encounter.[14] In the case of pTDE, the power law of the fallback rate is predicted to be steeper, $\propto t^{-9/4}$,[15] compared with complete disruption, $\propto t^{-5/3}$.[16] Furthermore, a remnant core has the potential to produce a second TDE if it becomes bound to the SMBH after the first encounter.[17]

A regular TDE usually refers to the stellar disruption by a single quiescent SMBH lying at the center of a galaxy.[10,16,18] However, special TDEs occurring in SMBH binaries (SMBHBs) have been proposed,[19] which exhibit interrupted tidal flares caused by the companion black hole, compared with the power law decay light curve (i.e., $\propto t^{-5/3}$).[16] SDSS J120136.02 + 300305.5 (hereafter SDSS J1201 + 30),[20] whose deep dips in its ∼ 300-day evolving X-ray light curve could be explained by the SMBHB TDE model, is the first SMBHB TDE candidate with a spectroscopic redshift of $z_{\mathrm{spec}} = 0.146$. Recently, a second X-ray candidate at $z_{\mathrm{spec}} = 0.1655$ with a ∼ 550-day X-ray light curve, OGLE16aaa, was reported.[21] Both SDSS J1201 + 30 and OGLE16aaa exhibit apparent interruptions in their soft X-ray light curves, which can be explained by the companion black hole perturbing the fallback rate of disrupted debris. The 0.2–2.0 keV X-ray flux

of SDSS J1201 + 30 decreased by more than 47 times within 7 days, while the 0.3–2.0 keV X-ray flux of OGLE16aaa increased by more than 63 times within 9 days. No intense hard X-ray emission was observed in either source.

To date, most X-ray TDEs have been discovered through the detection of soft X-ray flares, produced by emission from the transient accretion disk formed after the circularization of stellar debris. Near peak luminosities, the X-ray spectra of these TDEs are well fitted by either a blackbody with a temperature of $kT_{bb} = 0.04 - 0.12$ keV or a power law with an index of $\Gamma_X = 4 - 5$, followed by a spectral hardening over time.[22] In addition, there is another rare population of X-ray TDEs characterized by much harder spectra, extremely high X-ray luminosities, and dramatic short-time variability.[18,23] They are believed to be produced by powerful relativistic jets aligned with our line of sight, rather than by accretion.

Here, we report an unusual X-ray transient, XID 935 ($RA_{J2000} = 53.248664°$, $Dec_{J2000} = -27.841828°$, with a 1-$\sigma$ positional accuracy of 0.3 arcsec), discovered in the deepest X-ray survey ever—the 7 Ms Chandra Deep Field-South (CDF-S)[24,25]—whose extraordinary observational properties make it the deepest X-ray-selected TDE candidate. We use a cosmology of $H_0 = 70$ km s^{-1} Mpc^{-1}, $\Omega_M = 0.27$, and $\Omega_\Lambda = 0.73$.

MATERIALS AND METHODS

X-ray data

Data reduction. The CDF-S[24] and Extended-CDF-S (E-CDF-S) (250-ks depth)[26,27] surveys include a total of 111 Chandra observations performed between 1999 and 2016. The XMM deep survey in the CDF-S (XMM-CDFS) (3-Ms depth)[28] consists of 33 observations carried out between 2001–2002 and 2008–2010. The Wide-CDF-S (W-CDF-S) (29-ks depth)[29] has one observation covering the position of XID 935. Table S1 lists the observation identification number (ObsID), date, exposure, and bin name of these X-ray observations. Observation 581 is not included in the CDF-S due to telemetry saturation, but XID 935 is located on CCD I0 which escaped this disaster. All CDF-S and XMM-CDFS observations cover the position of XID 935. The E-CDF-S consists of four distinct sub-fields with only the edges overlapping between them, so only three (ObsIDs = 5021, 5022, and 6164) out of its nine observations observed XID 935 and are included in this work. ROSAT[30] and Swift[31] observations are listed in Table S2.

CIAO 4.14 with CALDB 4.9.7 was utilized to process the cleaned event files from the 7-Ms CDF-S[24] and E-CDF-S.[27] The *dmellipse* of CIAO was used to generate an elliptical source region that encloses 90% of the flux. The background region is an annulus with an inner radius of $R_{in} = 12''$ and an outer radius of $R_{out} = 40''$. According to the 7-Ms CDF-S catalog, six sources were masked since they are immediately adjacent to the background region of XID 935, as shown in Figure S2. In certain observations, the background region overlapped with the CCD gap, and these areas were masked using box regions. Spectral files were generated by the CIAO tool *specextract* and combined using *combine_spectra* according to the time bins specified in Table S1. The parameter *correctpsf* in *specextract* was set to yes for aperture correction.

SAS 21.0.0 was utilized to obtain cleaned event files of XMM-CDFS observations following the threads of *sas-thread-startup*, *sas-thread-epic-reprocessing*, and *sas-thread-epic-filterbackground*. Subsequently, the spectra were extracted using the spectral analysis threads of MOS (*sas-thread-mos-spectrum*) and PN (*sas-thread-pn-spectrum*). The source region is a circle with a radius of 10″ (corresponding to 60% encircled energy at 1.5 keV), and the background region is an annulus with an inner radius of $R_{in} = 25''$ and an outer radius of $R_{out} = 60''$. According to the 7-Ms CDF-S catalog, nine sources were masked with a circle with a radius of 20″, since they overlap with the background region of XID 935, as shown in Figure S3. The *arfgen* applied default aperture corrections for point sources. The spectral combination was performed using the SAS tool *epicspeccombine* according to the time bins listed in Table S1.

Xselect of HEASoft was used to extract the spectra from the event files of ROSAT and Swift (see Table S2 for ObsIDs). XID 935 is not detected in the ROSAT All-Sky Survey (RASS) observations conducted between June 1990 and August 1991. For Swift, the source region is a circle with a radius of $R = 30''$ and the background region is an annulus with an inner radius of $R_{in} = 40''$ and an outer radius of $R_{out} = 80''$. For ROSAT, the region configuration is the same as that of Swift, but $R = 60''$, $R_{in} = 70''$, and $R_{out} = 120''$. The arf file was generated using *xrtmkarf* of HEASoft for Swift, with a setting parameter *psfflag* = *yes* to correct the point spread function for point-like sources. The *pcarf* of HEASoft was used to generate the arf file for ROSAT, with an aperture correction factor of 0.94 based on the encircled energy function. For eROSITA,[32] the eROSITA-DE Data Release 1 archive supports a tool for the upper limit for a single position.

Bin strategies. The significance of source detection is calculated using the likelihood-ratio test[33] (see Listing S1). For p values larger than 0.0027, the flux/luminosity is considered as the upper limit at the 90% confidence level. For p values below this threshold (i.e., $\geq 3\,\sigma$), the flux/luminosity is reported as the mean value with a 1-σ uncertainty. Two different binning strategies for the light curve are applied to the Chandra and XMM-Newton data:

One-month binning.

(1) For both Chandra and XMM-Newton observations, a 1-month-bin scheme is initially applied for a straightforward overall view of the light curves (see Figure S4 for a flow diagram; Figure S5 for the 1-month-bin light curves).

Adaptive binning.

(1) Observations are marked as detected points if the significance of likelihood-ratio test in the full band is greater than 3-σ, and as non-detected points if the significance is less than 3-σ.
(2) For non-detected points, a 1-month-bin scheme is applied, but it stops at any detected point (see Figure S6 for a flow diagram). New bins are marked as non-detected points if the significances of likelihood-ratio tests in the full, soft, and hard band are all less than 3-σ; otherwise, they are marked as detected points.
(3) For detected points (both from step 1 and step 2), a 1-month-bin scheme is applied, but it stops at any non-detected point. If the right margin of a bin coincides with the exposure duration of a point, the right margin is set as the start time of that point.
(4) Some data remain non-detection even after 1-month binning. For these non-detected points, a 4-month-bin scheme is applied, but it stops at any detected point. New bins are marked as non-detected points if the significances of likelihood-ratio tests in the full, soft, and hard band are all less than 3-σ; otherwise, they are marked as detected points.

Spectral fitting. Given that XID 935 has low counts in most observations, it is not suitable to fit those spectra. The *aprates* of CIAO is used to calculate the count rate, then *modelflux* of CIAO is used to calculate the flux using this count rate, and subsequently the luminosity is derived from this flux. For *modelflux*, the parameters *model* = *xspowerlaw.pow*1, *absmodel* = *xsphabs.abs*1, *absparams* = *abs*1.*nH* = 0.008,[34] and *paramvals* = *pow*1.*PhoIndex* = 2.4 are based on the spectral fitting result through stacking all XID 935 Chandra observations. The cosmology model is set as the default one in XSPEC. Figure 1 shows the adaptive-bin scheme light curves (data listed in Table S4).

Spectral fitting is only performed for the spectrum with net counts larger than 60 (see Table S3; Figure S7). To fit the spectrum for a weak source, especially with low counts in its background, a better grouping strategy is to ensure that each bin in the background spectrum contains at least one count to use the W statistic.[35] The HEASoft tool *ftgrouppha* supports this grouping by setting the parameter *grouptype* = *bmin* and *groupscale* = 1. The XSPEC 12.13.0 software was used to fit the regrouped spectra derived from both Chandra and XMM-Newton observations. We apply a Galactic and intrinsic absorbed redshifted power law model, *tbabs* × *ztbabs* × *zpowerlw*, to the spectra of XID 935, with the Galactic column density fixed at $N_H = 8.8 \times 10^{19}$ cm^{-2}, redshifts of *zpowerlw* and *ztbabs* fixed at $z = 0.251$, power law photon index, and redshifted N_H left free to vary. The best-fit column density during these bins was always $N_H < 10^{22}$ cm^{-2} (see exclusion of a variable absorption origin), which implies that the absorption is not severe in these periods.

UV/optical data

The UV/optical observations of XMM/OM and Swift/UVOT were performed for XID 935. The HEASoft tool *uvotimsum* was utilized to sum the Swift/UVOT UV/optical observations and the SAS tool *ommosaic* was used to sum the XMM/OM UV/optical observations. Photutils[36] was used to perform aperture photometry (a circle with a 4″ radius for the source region; an annulus with a 6″ inner radius and a 10″ outer radius for the background region) on the summed UV/optical images. The aperture correction factors are 0.65, 0.7, 0.7, and 0.8 for XMM/OM UVW2, UVM2, UVW1, and u bands, respectively. For Swift/UVOT UVW2, UVM2, UVW1, and u bands, the aperture correction factor is all 0.95. The results are shown in Figure S1.

Host SED fitting

The spectral energy distribution (SED) fitting was performed using CIGALE[37] with the following multi-wavelength data: *WFI_B*, *WFI_V*, *WFI_R*, *WFI_I*, *WFI_z*, *WFI_J*, *WFI_H*, *WFI_K*, *spitzer.irac.ch*1 (3.6 μm), *spitzer.irac.ch*2 (4.5 μm), *spitzer.irac.ch*3 (5.8 μm), *spitzer.irac.ch*4 (8.0 μm),[38] *spitzer.mips*.24 (24 μm),[39] *spitzer.mips*.70 (70 μm),[40] *scuba*.850 (850 μm),[41] and *Swift_ UVOT.UVW*2, *Swift_UVOT.UVM*2, *Swift_UVOT.UVW*1, *Swift_UVOT.U* bands obtained as described in UV/optical data. For each band, based on A_f/A_v (SVO Filter Profile Service: http://svo2.cab.inta-csic.es/theory/fps/) and $A_v = R_v \times E(B-V)$, setting $E(B-V) = 0.0072$, assuming $R_v = 3.1$, the A_v has been calculated and applied in Galactic extinction correction. Table S6 lists the CIGALE parameters used in our fitting and Figure 2 shows the fitting result.

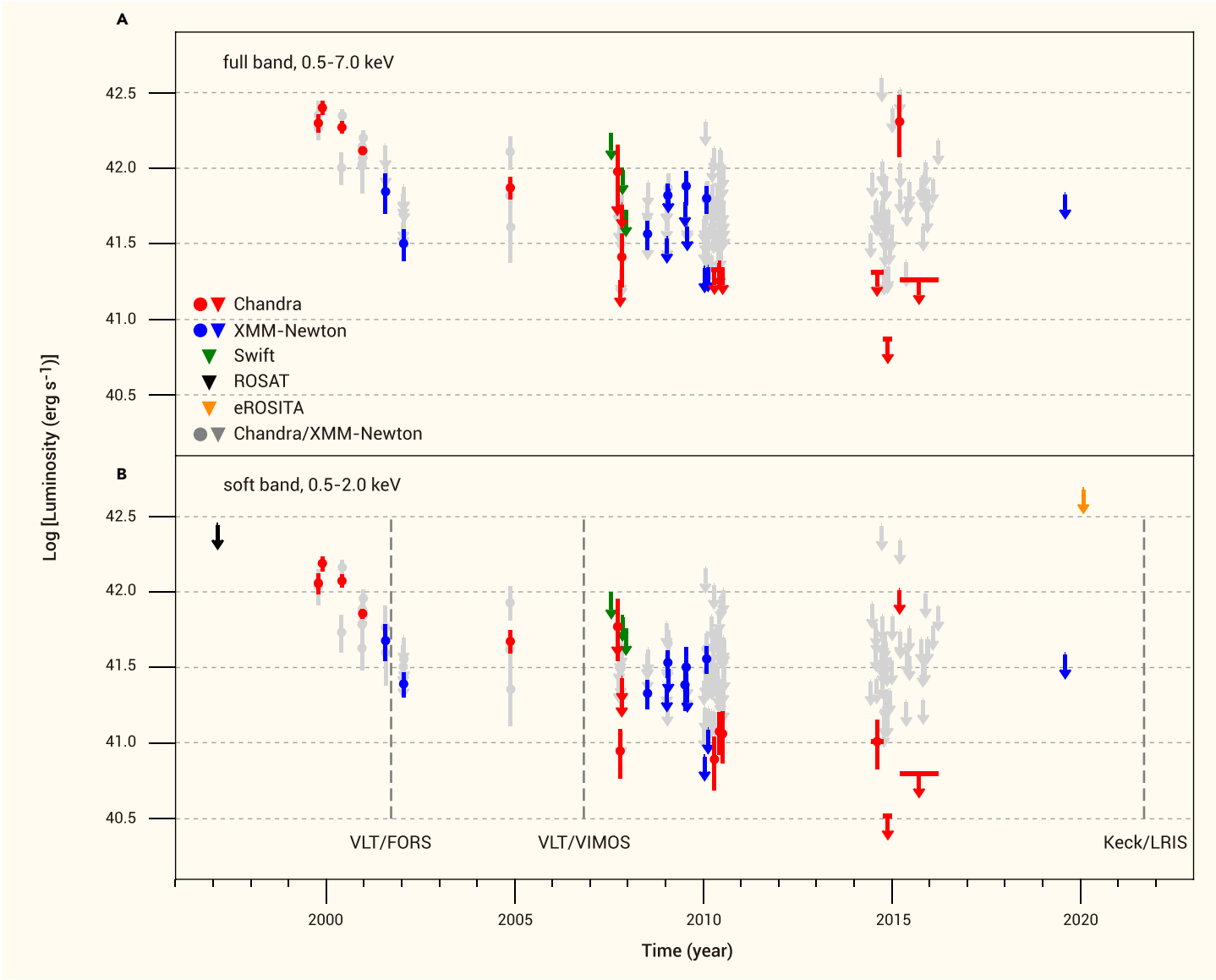

Figure 1. Adaptive-bin X-ray light curves of XID 935 (A) Light curve in the rest-frame 0.5–7.0 keV band (full band, containing **768.9** ± **43.3** and **905.0** ± **84.0** Chandra and XMM-Newton net counts, respectively). (B) Light curve in the rest-frame 0.5–2.0 keV band (soft band, containing **595.9** ± **28.5** and **680.7** ± **62.6** Chandra and XMM-Newton net counts, respectively). Red, dark blue, green, black, and orange data are from Chandra, XMM-Newton, Swift, ROSAT, and eROSITA, respectively. Gray data represent individual observations of Chandra and XMM-Newton. Horizontal bars indicate ranges of time bins. Arrows indicate 90% confidence level upper limits. The data gaps between 2002–2004 and 2005–2007 indicate no X-ray observational coverage. Dashed lines denote the observation times of optical spectra.

We use GALFIT[42] to decompose the bulge and disk components of images in the *WFI_B*, *WFI_V*, *WFI_I*, and *WFI_z* bands. SED fitting for the bulge reveals no significant difference from the total galaxy.

Optical spectral reduction

To pin down the nature of XID 935, whose temporal evolution could be due to the AGN variability, we obtained an optical spectrum of the source with the Keck I telescope at the W.M. Keck Observatory and the low-resolution imaging spectrometer (LRIS)[43] on UT2021-09-08 14:30 (MJD 59465.6045). A total of 850 s and 450 s × 2 exposures were obtained through the LRIS blue- and the red-arm CCDs, respectively. The combination of the 5,600 Å dichroic, the 600/4,000 blue grism (with a 0.63 Å pixel^{-1} dispersion), and the 400/8,500 red grism (with a 1.20 Å pixel^{-1} dispersion), together with a 1″ slit width provided an observed wavelength coverage of 3,150–10,270 Å. The spectral resolution near the central wavelength of the blue and the red arms yields, $R_{blue} \sim 942$ and $R_{red} \sim 844$, corresponding to ∼4.7 and ∼9.4 Å resolution element in the blue and the red arms, respectively. During the observation, the slit was aligned to the parallactic angle, which is ≈ − 5° from the North. The raw LRIS spectral data were processed by the fully automated LPipe pipeline.[44] The spectra were dominated by absorption lines without prominent emission lines, indicating the absence of significant AGN activity. To assess the upper limits of AGN activity, we calculated the upper limits of [OIII] as follows. The Keck/LRIS spectrum was first corrected for Galactic extinction using the dust map of Schlafly et al.[45] and the extinction curve from Fitzpatrick et al.[46] The starlight continuum was then modeled using the Python package pPXF of Cappellari and Emsellem[47] and Cappellari,[48] which enables the extraction of stellar population and kinematics through penalized fitting. Figure 3 shows the optical spectra.

After subtracting the modeled continuum from the spectrum, we calculated the [OIII] upper limits at a 90% confidence level using the method outlined in Avni,[51] assuming a pseudo-width of [OIII] from composite spectra of Vanden et al.[52]

Numerical modeling

To verify whether the SMBHB TDE model can explain the observed results, we conducted a series of numerical simulations for comparison with the observational data. The numerical model is based on three-body scattering experiments. Here, we briefly introduce our modeling approach. For more details, please refer to Liu et al.[19,20]

We assume that a star on a parabolic orbit is tidally disrupted at the pericenter r_p. The specific energy E of the stellar debris after disruption ranges from $-E_b - \Delta E$ to $-E_b + \Delta E$, where E_b is the orbital binding energy of the star, and ΔE is the spread in specific energy.[10,53] For a star on the parabolic orbit, nearly half of the debris is bound to the SMBH after the tidal disruption. As a result, the specific energy of the bound debris ranges from $-\Delta E$ to 0. We assume that the disrupted star is constructed as polytropes with a solar mass. And the mass distribution of the debris can be assumed to be constant.[53] To simplify

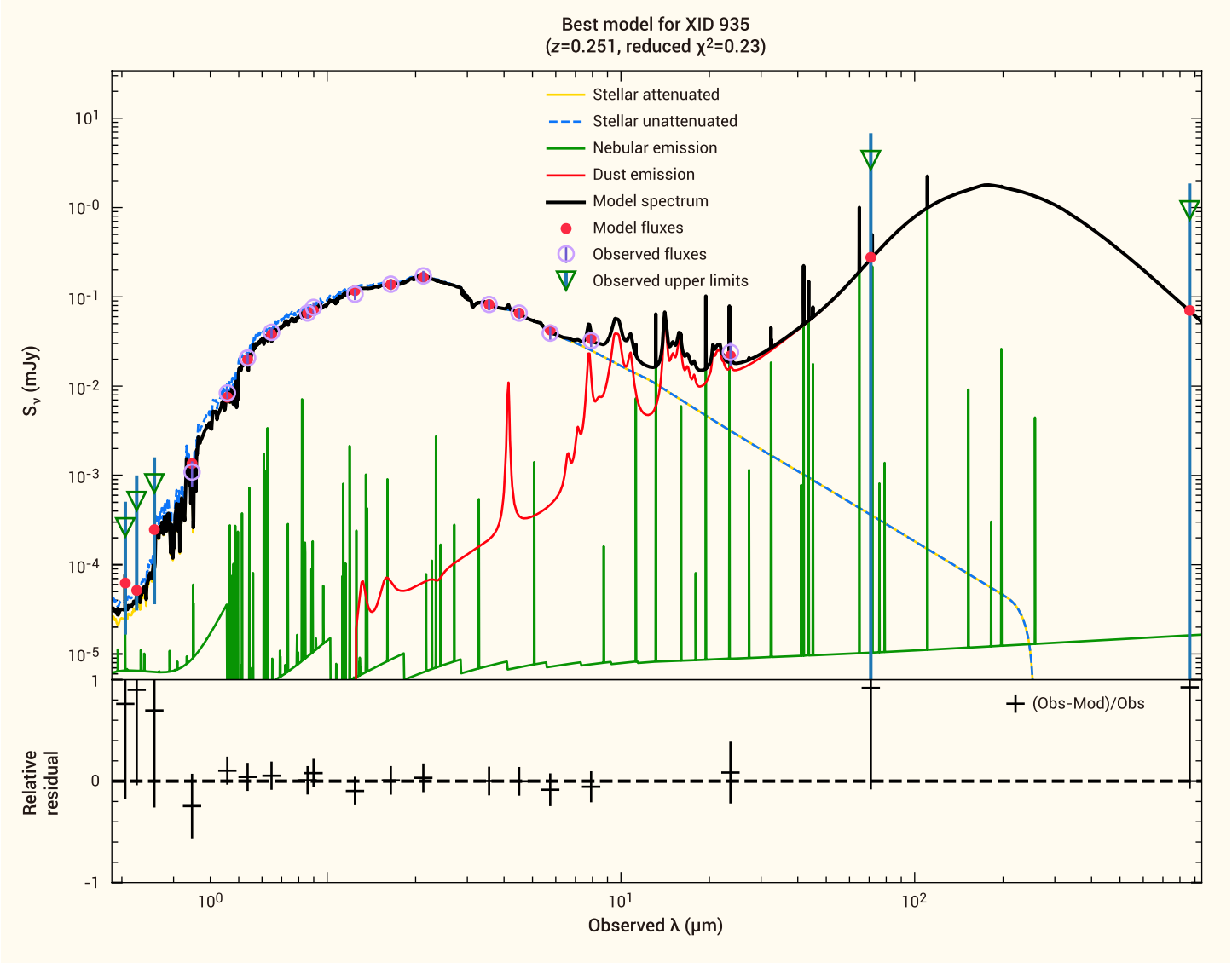

Figure 2. SED fitting result for XID 935 using CIGALE The stellar mass $M_{\star}$ = (3.1 ±0.6) × 10^{10} $M_{\odot}$ and the star formation rate (SFR) < 1.3 × $10^{-2}$$M_{\odot}$/year (90% confidence level) were obtained. Note that an AGN component is not required in the fitting.

the calculation, we neglect the interactions between debris elements. As a consequence, each element follows a ballistic trajectory. Thus we can perform scattering experiments for each three-body system composed of the binary black holes and the debris element. Although this simplification is less precise than full hydrodynamical simulations, it provides a sufficiently accurate approximation for order-of-magnitude estimates and qualitative analysis.

From the scattering experiment results, it is easy to estimate the rate at which the debris returns to the vicinity of the black hole, namely the mass fallback rate. Assuming that the fallback rate is proportional to the X-ray emission, we can make the conversion factor η as a free parameter and fit it to the observed flux. By comparing the "light curve" derived from the scattering experiments (more precisely, the fallback curve) with the observational data, we can infer the approximate time of disruption based on the position of the peak along the time axis. This gives us $T_{\rm delay}$, the delay between the actual disruption and the first effective observational detection.

It should be noted that the methodology described above may lead to multiple sets of parameters that fit the data. Our analysis serves to qualitatively evaluate the plausibility of the SMBHB TDE model in explaining the observations, rather than to exactly determine the system's actual orbital parameters.

RESULTS AND DISCUSSIONS

Light curves and spectra

XID 935 was originally detected in the first 1-Ms observations of the CDF-S,[54] with an optical counterpart subsequently classified as an inactive galaxy showing only absorption lines with $z_{\rm spec}$ = 0.251 based on a VLT/FORS optical spectrum obtained on September 18–20, 2001[50] as shown in Figure 3. Luo et al.[24] classified XID 935 as an AGN based on the entire 7-Ms CDF-S data. Zheng et al.[55] found six candidate transients based on the criterion that the flux change exceeds 3-σ of the average flux, using the 3-month bin 7-Ms CDF-S light curves. Three of these candidates (XID 725,[56] XID 330,[57] and XID 403[58]) have been reported in the literature. XID 935 is among these six candidate transients and is reclassified as a long outburst transient. XID 935 was additionally observed as part of the E-CDF-S (250-ks depth),[26,27] the XMM-CDFS (3-Ms depth),[28] the W-CDF-S (29-ks depth),[29] Swift (0.5-Ms depth),[31] ROSAT (8.52-ks depth),[30] and eROSITA (0.218-ks depth),[32] providing relatively well-sampled 20-year-long X-ray light curves of XID 935. Unlike the 3-month bin scheme adopted by Zheng et al.,[55] we use an adaptive-bin scheme to obtain light curves (see Figure 1; data listed in Table S4), given that some interrupted flares that are shorter than the 3-month timescale will be smoothed out and that stacking adjacent non-detection observations could increase the detection sensitivity.

Below, we summarize the observational features of XID 935.

(1) A peak soft X-ray luminosity of $L_{0.5-2\ \rm keV}$ = $10^{42.14\pm0.04}$ erg s^{-1} was recorded in October–November 1999, dimming by a factor of at least 40 between November 1999 and October 2014.

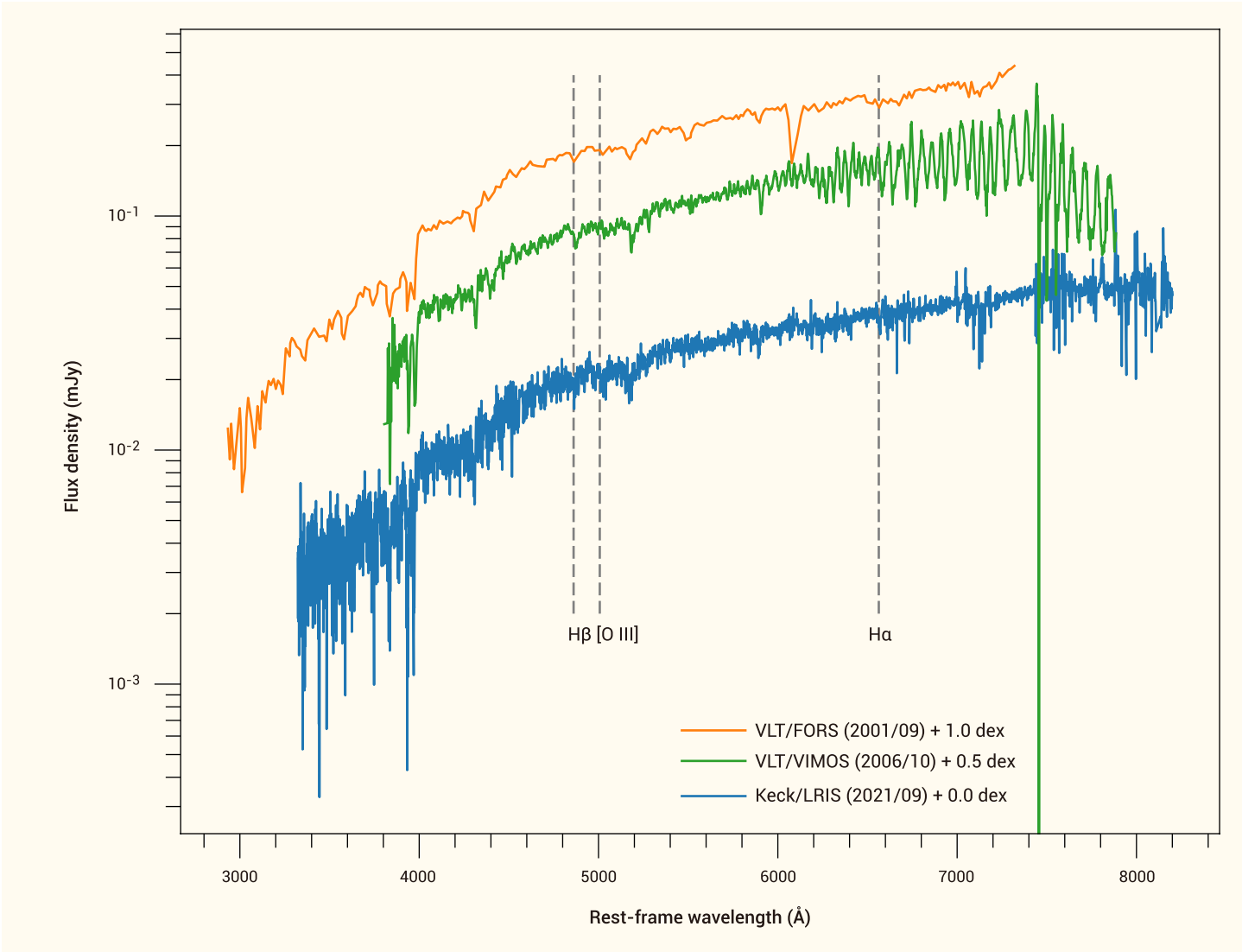

Figure 3. Optical spectra of XID 935 The spectral analysis of the Keck/LRIS spectrum (blue), performed on September 8, 2021, shows that the host galaxy of XID 935 has no significant AGN characteristics. The flux upper limit of the [OIII] emission line is $10^{-16.68}$ erg s^{-1} cm^{-1} and the stellar velocity dispersion is 138 ± 31 km/s. The VLT/VIMOS spectrum (green) was obtained on October 30, 2006.[49] The VLT/FORS spectrum (orange) was observed on September 18–20, 2001.[50]

(2) Significant hard X-ray emission of $L_{2-7\ \mathrm{keV}} = 10^{42.09\pm0.12}$ erg s^{-1} was detected in November 1999; however, there was almost no detection ($<3\sigma$) of hard X-ray emission after December 2000 except on March 16, 2015.

(3) It displays extreme and fast luminosity variations: the full-band (0.5–7.0 keV) X-ray luminosity increased by a factor of at least 27 within ~ 2 months, from a 90% confidence level upper limit of $L_{0.5-7\ \mathrm{keV}} < 10^{40.87}$ erg s^{-1} (October 10, 2014–January 4, 2015) to $L_{0.5-7\ \mathrm{keV}} = 10^{42.31\pm0.20}$ erg s^{-1} (March 16, 2015).

(4) The X-ray emission is centered in the host galaxy, with no AGN characteristics (see Figure 3) or UV/optical variability (see Figure S1).

(5) No radio emission was detected at 15 mm,[59] 6 cm,[60] 13 cm,[61] 21 cm,[62–66] 92 cm,[67] 1.25–3.75 m,[68] 1.5–3 m,[69] and 4 m bands,[70] as well as the very large array (VLA) survey of the CDF-S,[71] the VLA Survey of the GOODS-S,[72] the ultradeep radio imaging of GOODS-S/HUDF,[73] and the VLA Sky Survey (VLASS),[74] with no jet being detected.

Exclusion of a variable absorption origin

The X-ray variability could be attributed to intrinsic spectral variation and/or variable absorption. For an absorbed power law model, with a power law photon index of $\Gamma = 2.4$ (derived from spectral stacking of Chandra observations listed in Table S1) and a column density of $N_{\mathrm{H}} = 1 \times 10^{22}$ cm^{-2}, a minimum of 60 full-band net counts are required for a reliable fit. However, since most of the bins for XID 935 have low counts, only seven bins contain full-band net counts exceeding 60, which are used to estimate the intrinsic absorption. A Galactic and intrinsic absorbed redshifted power law model, *tbabs* × *ztbabs* × *zpowerlw*, is applied to these seven spectra, with the Galactic column density fixed at $N_{\mathrm{H}} = 8.8 \times 10^{19}$ cm^{-2}[34] and the redshift fixed at $z = 0.251$.[50] The power law photon index and the redshifted N_{H} are allowed to vary freely. The best-fit column density in these seven bins (see Table S3) was always less than 10^{22} cm^{-2}. If the X-ray variability were primarily driven by varying obscuration, a harder spectrum would be expected, as soft photons would be absorbed. However, after 2001, most bins of XID 935 show no detection in the hard band but significant detection in the soft band, suggesting a preference for soft spectra. When both the soft and hard bands show non-detection, it becomes challenging to disentangle the contribution from intrinsic spectral variation and variable absorption. Notably, the optical spectra of XID 935 show no characteristics of AGN activity, implying that there is little surrounding matter near the black hole. Hence, we assume that the X-ray variability of XID 935 is not caused by the variable absorption, and a Galactic-absorbed redshifted power law model, *tbabs* × *zpowerlw*, with fixed $N_{\mathrm{H}} = 8.8 \times 10^{19}$ cm^{-2}, $\Gamma = 2.4$, and $z = 0.251$, is adopted to estimate the flux and luminosity (see materials and methods).

Exclusion of an AGN origin

It is not uncommon for AGNs to vary in brightness by several dozen times, either due to intrinsic spectral variation or variable absorption. Such sources typically exhibit persistent AGN signatures revealed by

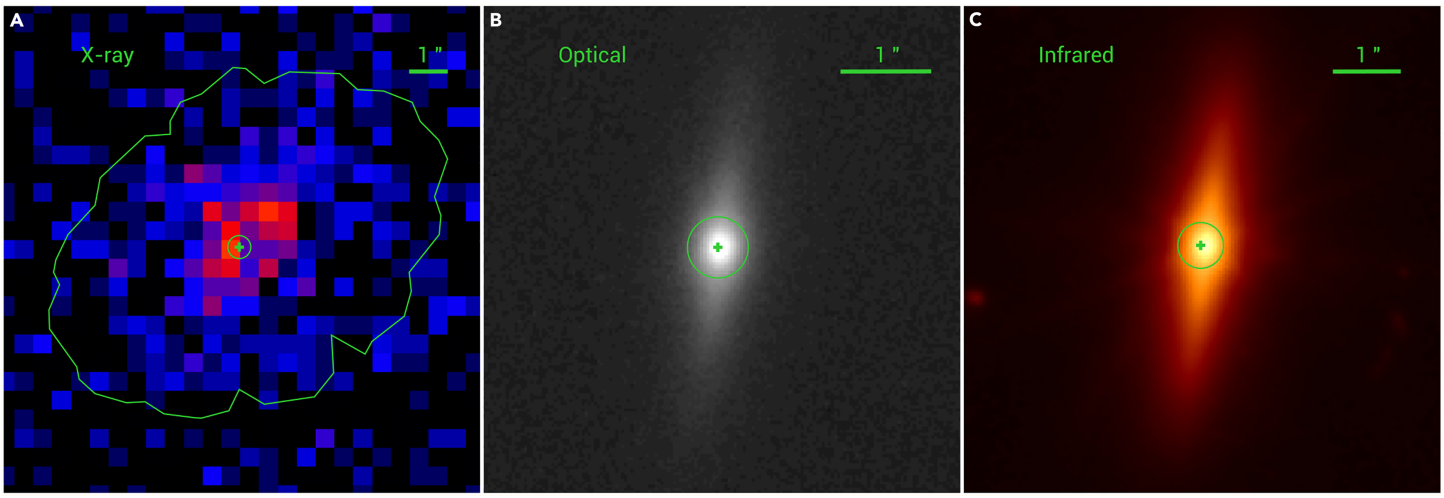

Figure 4. Multi-wavelength images of XID 935 (A) CDF-S image (7 Ms) in the observed 0.5–7.0 keV band, with total net counts of **768.9 ± 43.3**. The green polygon is the 90% encircled energy fraction region, centered at the source position (green plus; with a 1-σ positional accuracy of 0.3 arcsec, indicated by the green circle, corresponding to 0.99 kpc at z = **0.251**). (B) GOODS z band image. (C) JWST-NIRCam F227W band image. The green pluses and circles in (B) and (C) are the same as that in (A). The position of XID 935 is consistent with the nucleus of its host galaxy.

the strong narrow emission lines in their optical spectra. However, optical spectra of XID 935 obtained with VLT/FORS in September 2001[50] and VLT/VIMOS in October 2006[49] reveal no apparent AGN signature. We utilized Keck/LRIS to obtain a new optical spectrum of XID 935 on September 8, 2021 (see Figure 3 and materials and methods), which also shows no AGN signature. From the Keck spectrum, we estimate the 90% confidence level flux upper limit of the [OIII] emission line, which is $f_{[OIII]} < 10^{-16.68}$ erg s^{-1} cm^{-2}. In addition, the ZTF r-band light curve shows no statistically significant variability over timescales of 5 years (see Figure S1). These findings suggest that the host galaxy of XID 935 is likely not an active galaxy. Some AGNs, known as "X-ray bright, optically normal galaxies" (XBONGs),[75] are X-ray bright but lack apparent AGN optical signatures. However, to our knowledge, no XBONG has shown X-ray variability by a factor of $\geq$ 40. Moreover, the AGN scenario fails to account for the rapid luminosity changes discussed in point (3) of Light curves and spectra, so we exclude this possibility from further consideration.

Exclusion of an X-ray binary origin

X-ray binary (XRB) populations could also be a possible origin of hard X-ray emission. Using the stellar mass [$M_\star = (3.1 \pm 0.6) \times 10^{10}\ M_\odot$] and the star formation rate ([SFR] < $1.3 \times 10^{-2} M_\odot$ year^{-1}, at the 90% confidence level) derived from SED fitting (see materials and methods), and applying the relationship between XRB X-ray luminosity, stellar mass, SFR, and redshift,[76] we estimate the contribution of XRB populations to the X-ray emission of XID 935 to be $L_{2-10\ keV}$(XRB) = $10^{40.22\pm0.30}$ erg s^{-1}. Apparently, this contribution is insufficient to account for the observed hard X-ray emission ($L_{2-7\ keV} \sim 10^{42}$ erg s^{-1}). Moreover, due to the large number of XRBs, these populations as a whole are not expected to exhibit significant variability. Essentially no known individual extragalactic ultraluminous X-ray sources (ULXs) exhibit the required luminosity of $L_{2-7\ keV} \sim 10^{42}$ erg s^{-1}, as ESO 243-49 HLX-1,[77] one of the most luminous ULXs known, attains only $L_{2-7\ keV} \sim 10^{41}$ erg s^{-1}. Given that the number of galaxies in the filed of view of 7-Ms CDF-S[24] reaches 50,539, the probability of a Galactic or local universe XRB aligning randomly with the core of a galaxy (within a 0.3″ radius) is about 0.79%. Therefore, XRB is not a reasonable explanation for XID 935.

TDE scenarios

Given the high level of its peak X-ray luminosity and its location at the center of its host galaxy, an edge-on disk galaxy (see Figure 4), it is reasonable to infer that the activity of XID 935 is linked to the central SMBH. As discussed above, the likelihood of XID 935 being an AGN is low. Consequently, a TDE emerges as a plausible scenario for XID 935.

Observationally, XID 935 is the observationally faintest X-ray-selected TDE candidate to date, as illustrated in Figure 5.

The current X-ray observational capabilities remain inadequate for detecting enough faint TDEs such as XID 935 at $z > 0.1$ to enable systematic investigation of such TDEs at different redshifts. Thanks to the best X-ray coverage spanning over 20 years with the deepest total exposure of $\sim$ 9.5 Ms, we can test the performance of TDE models on both long timescales and fine structural details.

Using the M_{BH}–$\sigma_\star$ relation[78] and stellar velocity dispersion $\sigma_\star = 138 \pm 31$ km s^{-1} measured from the Keck optical spectrum, we estimated an SMBH mass of $M_{BH} = 10^{7.45\pm0.88}\ M_\odot$. A non-spinning SMBH with this mass can effectively tidally disrupt a main-sequence star (see Figure 1 in Gezari[79]).

The full-band X-ray luminosity of XID 935 increased by a factor of at least 27 within $\sim$ 2 months, from a 90% confidence level upper limit $L_{0.5-7\ keV} < 10^{40.87}$ erg s^{-1} (October 10, 2014–January 4, 2015) to $L_{0.5-7\ keV} = 10^{42.31\pm0.20}$ erg s^{-1} (March 16, 2015). Table 1 shows the comparison between XID 935 and the two aforementioned SMBHB TDE candidates.

Remarkably, the March 16, 2015, detection showed a significance of 3.16σ. It is challenging for both regular TDEs and AGNs to generate such notable luminosity changes within such short time frames,[79,80] making the March 16, 2015, detection more appropriately treated as anomalous cases in both scenarios. However, SMBHB TDEs could bring about such alterations in the accretion state due to the companion black hole perturbing the fallback rate of disrupted debris.[20] Indeed, the SMBHB TDE model[19] can qualitatively describe the main trend of the XID 935 soft-band light curve, with three example sets of parameters being favored by the observations (see Figure 6 and numerical modeling for details).

These results show different time delays (T_{delay}) between the first observational detection point and the moment of TDE occurrence, different ellipticities of SMBHB orbit, the same primary SMBH of $M_{BH} = 2.0 \times 10^7\ M_\odot$, different mass ratios between the secondary and primary SMBHs, different penetration factors, and the same orbital period of the SMBHB (see Liu et al.[20] for more details about parameters). The relatively smooth decays observed in 2000–2002 and 2008–2010 could be reasonably explained by the regular TDE accretion stage in the SMBHB TDE model. The drop in 2015–2016 can be attributed to the perturbation of the TDE streams by the companion SMBH. However, this SMBHB TDE model is based on a simplified assumption that the bound debris of the TDE is regarded as free-moving particles, ignoring self-gravity and pressure. Hence, it cannot predict the fine structures of the light curve after several orbital periods, e.g., the fluctuations during January–July 2009 and drop during September–November 2007 (see Figure 6). A more physical SMBHB TDE model capable of explaining the fine structures of the light curve is desired. Additionally, the data gaps (i.e., no observational coverage) between 2002–2004 and 2005–2007 further complicate model validation.

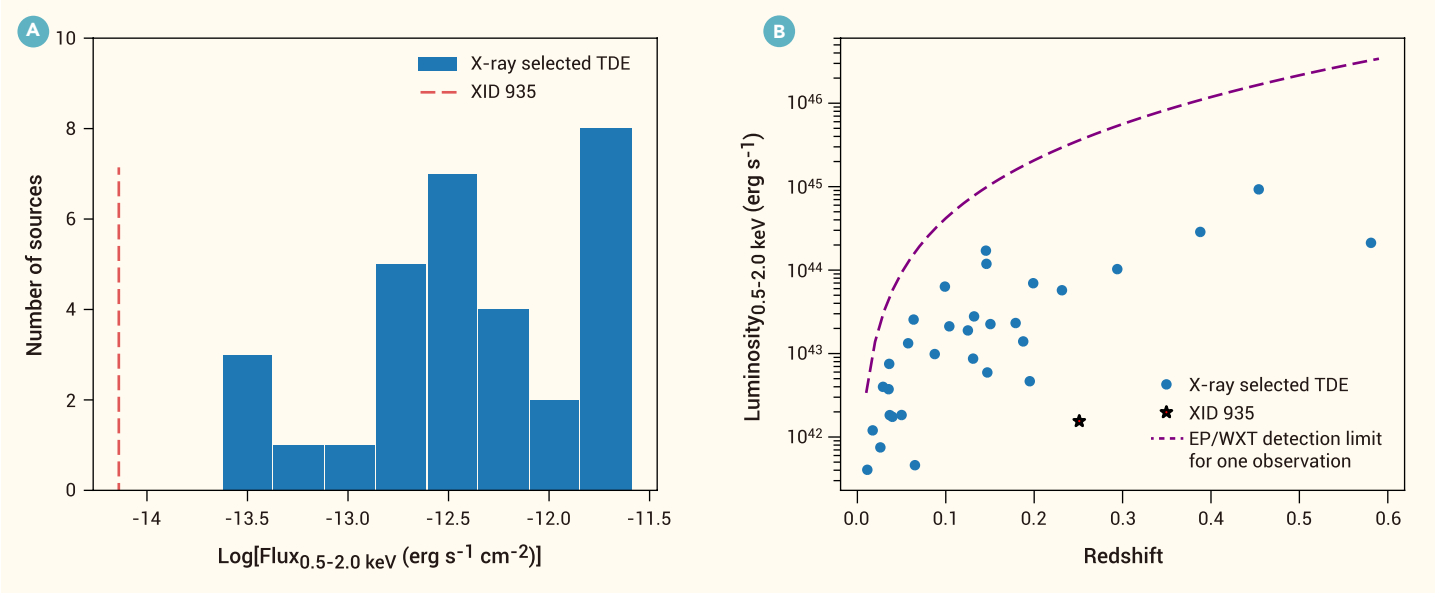

Figure 5. X-ray-selected TDEs (A) Distribution of absorption-corrected peak 0.5–2.0 keV fluxes of X-ray-selected TDEs, with the vertical red dashed line highlighting XID 935. (B) Absorption-corrected peak 0.5–2.0 keV luminosities as a function of redshift, with XID 935 marked with a star symbol and other X-ray-selected TDEs represented by blue points. The purple dashed curve is the 5-σ detection limit of EP/WXT in an individual observation (i.e., 1.2-ks exposure).

The light curve of XID 935 during 1999–2002 shows a relatively smooth and steep ($\propto t^{-2.38}$) decline, suggesting a likely pTDE ($\propto t^{-9/4}$).[15] In contrast to complete disruption, a stellar core survives in the pTDE scenario, leading to a fallback rate that is steeper than $t^{-5/3}$. The circularization process[81–83] seems to be a possible interpretation of the early behavior of XID 935 during 1999–2002. However, in the circularization process, even a black hole with a low mass of $M_{\rm BH} = 10^6\ M_\odot$ would not sustain a 1,000-day decline. Given that XID 935 has $M_{\rm BH} \sim 10^{7.45\pm0.88}\ M_\odot$, the circularization process is expected to be highly efficient, with a timescale described by

$$t_{\rm cir} = 7\,\beta^{-4}\left(\frac{M_{\rm BH}}{10^{7.45}\,M_\odot}\right)^{-7/6}\left(\frac{M_*}{M_\odot}\right)^{-4/3}\left(\frac{R_*}{R_\odot}\right)^{7/2}\ \text{days}. \quad \text{(Equation 1)}$$

$t_{\rm cir}$ is given by the combination of Equations 4 and 10 in Chen and Shen.[83] Consequently, circularization is unlikely to be the primary mechanism driving the flare observed in XID 935. Nevertheless, the efficient circularization suggests that stream-stream collisions could rapidly lead to the formation of a compact accretion disk. As a result, the X-ray emission is predominantly governed by the disk accretion process. Furthermore, the hard X-ray spectrum observed during the early phase appears to originate from the accretion disk or its corona, rather than from the circularization process, which is typically associated with optical/UV emission rather than X-rays.[84]

CONCLUSION

We report on a TDE candidate, XID 935, in the 7-Ms CDF-S. XID 935 has the faintest peak 0.5–2.0 keV X-ray flux among all X-ray-selected TDEs discovered to date. Thanks to the best X-ray coverage spanning over 20 years with the deepest total exposure of ~ 9.5 Ms, its relatively well-sampled and long-timescale light curves enabled testing of existing TDE models. A TDE by a single SMBH or a pTDE scenario cannot explain the primary trend of the XID 935 light curves. In contrast, the SMBHB TDE model successfully reproduces the overall behavior of the light curves; however, it still fails to match short-timescale fluctuations exactly. Therefore, the exceptional observational features of XID 935 provide a key benchmark for refining quantitative TDE models and simulations. Ongoing time-domain X-ray surveys conducted by facilities such as the Einstein Probe[85,86] may significantly enlarge the sample of X-ray TDEs, alongside XID 935, further enriching our knowledge of TDEs and their underlying physics.

RESOURCE AVAILABILITY

Materials availability

This study did not generate new unique materials/reagents.

Data and code availability

- Raw data for the observations taken with Chandra, XMM-Newton, ROSAT, and Swift are available through the HEASARC online archive services: https://heasarc.gsfc.nasa.gov/docs/archive.html.
- The authors can provide other data supporting the findings of this study on request.

FUNDING AND ACKNOWLEDGMENTS

This work is supported by the National Key R&D Program of China (2023YFA1608100 and 2022YFF0503401), NSFC grants (12025303 and 12393814), and the Strategic Priority Research Program of the Chinese Academy of Sciences (XDB0550300). S.L. acknowledges the support by the National Science Foundation of China under grant NSFC no. 12473017. F.E.B. acknowledges support from ANID-Chile BASAL CATA FB210003, FONDECYT Regular 1241005, and Millennium Science Initiative Program – ICN12_009. J.-H.C. acknowledges the support from the National Natural Science Foundation of China (grant no. 12503053). The funders had no role in study design, data collection and analysis, decision

Table 1. Comparison between XID 935 and previous SMBHB TDE candidates

-	XID 935	SDSS J1201 + 30	OGLE16aaa
Redshift	0.251	0.146	0.1655
Dimming degree	> 11 times (within 3 days)	> 47 times (within 7 days)	–
Flaring degree	> 27 times (within 70 days)	–	> 63 times (within 9 days)
Hard X-ray emission	yes	no	no
Optical/UV variability	no	no	Yes

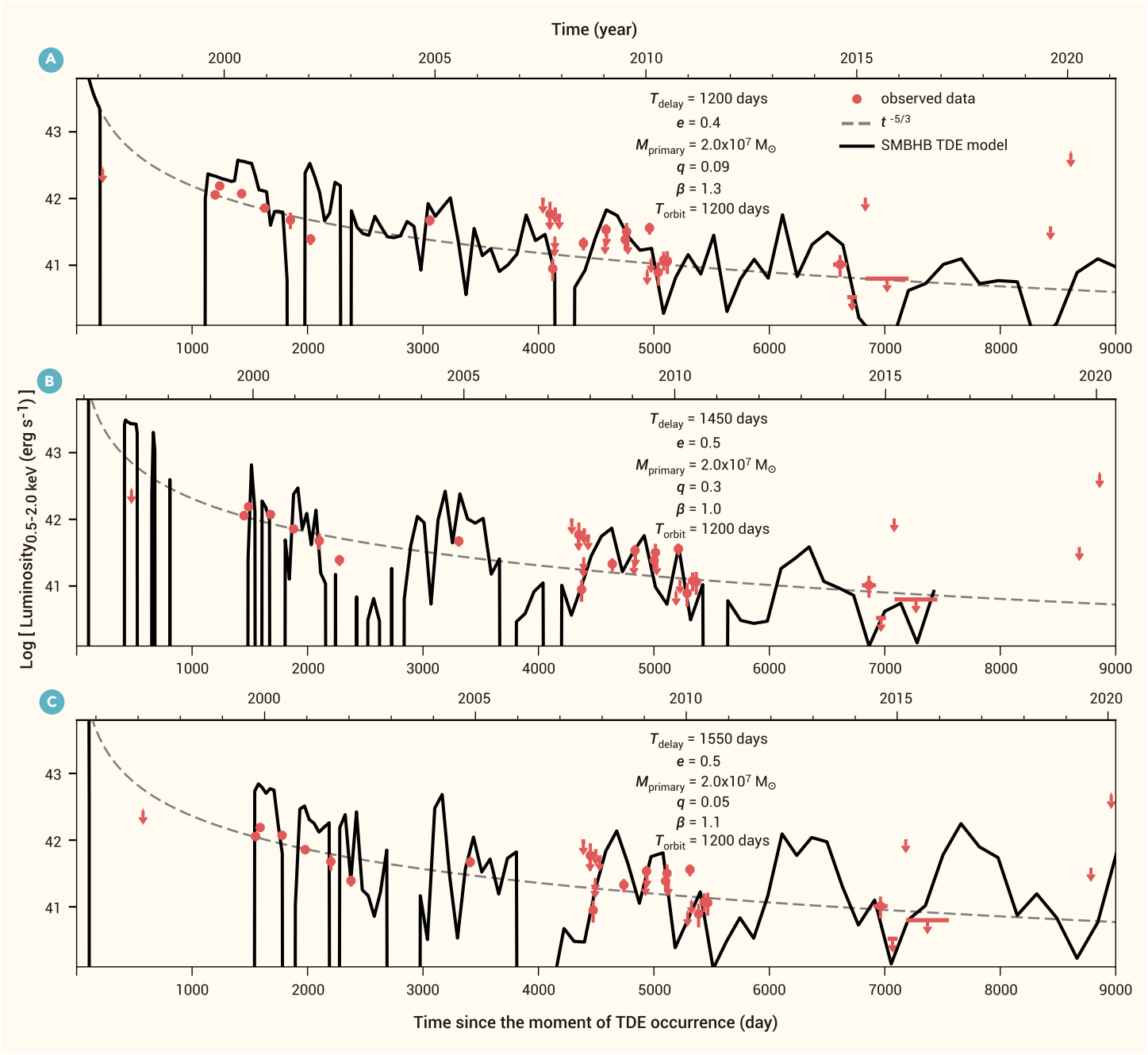

Figure 6. SMBHB TDE model fits for XID 935 In each panel, the rest-frame 0.5–2.0 keV light curve is shown with red symbols. Error bars correspond to 1-σ uncertainties. Downward arrows are 90% confidence level upper limits. The dashed gray curve represents the canonical $t^{-5/3}$ decay law. The gapped black solid curve is the SMBHB TDE model fitting result, with the following model parameters annotated: T_{delay}, the time delay between the first observed detection data point and the moment of TDE occurrence; e, the ellipticity of SMBHB orbit; $M_{primary}$, the mass of the primary black hole; q, the mass ratio between the secondary and primary SMBHs; β, the penetration factor; T_{orbit}, the orbital period of SMBHB. (A) T_{delay} = 1200 days, e = 0.4, q = 0.09, β = 1.3. (B) T_{delay} = 1450 days, e = 0.5, q = 0.3, β = 1.0. (B) T_{delay} = 1550 days, e = 0.5, q = 0.05, β = 1.1. (A), (B), and (C) share identical values of $M_{primary} = 2.0 \times 10^7 M_{(\cdot)}$ and T_{orbit} = 1200 days.

to publish, or preparation of the manuscript. Many thanks to W.N. Brandt for his valuable comments on this manuscript.

AUTHOR CONTRIBUTIONS

Y.X. designed the project. M.H. analyzed the Chandra, XMM-Newton, and Swift data, and performed SED fitting. M.H. and Y.X. wrote the manuscript. S.L. and F.L. constructed the SMBHB TDE model. J.-H.C. and R.-F.S. constructed the pTDE model. Y.Y. and N.J. obtained the new Keck/LRIS optical spectrum. Y.W. analyzed the Keck/LRIS optical spectrum. All authors contributed to the manuscript and approved the final version.

DECLARATION OF INTERESTS

Y.X. is a member of The Innovation's scientific advisory board and was blinded from reviewing or making final decisions on the manuscript. Peer review was handled independently of this member and their research group.

SUPPLEMENTAL INFORMATION

It can be found online at https://doi.org/10.1016/j.xinn.2025.101169.

LEAD CONTACT WEBSITE

Mengqiu Huang: https://orcid.org/0009-0003-5280-0755
Yongquan Xue: https://orcid.org/0000-0002-1935-8104

REFERENCES

1. Schmidt, M. (1963). 3C 273 : A Star-Like Object with Large Red-Shift. *Nature* **197**:1040. DOI:10.1038/1971040a0
2. Hills, J.G. (1975). Possible power source of Seyfert galaxies and QSOs. *Nature* **254**:295–298. DOI:10.1038/254295a0
3. Young, P.J., Shields, G.A. and Wheeler, J.C. (1977). The black tide model of QSOs. *Astrophys. J.* **212**:367–382. DOI:10.1086/155056

4. Frank, J. (1978). Tidal disruption by a massive black hole and collisions in galactic nuclei. *Mon. Not. Roy. Astron. Soc.* **184**:87–99. DOI:10.1093/mnras/184.1.87
5. Magorrian, J. and Tremaine, S. (1999). Rates of tidal disruption of stars by massive central black holes. *Mon. Not. R. Astron. Soc.* **309**:447–460. DOI:10.1046/j.1365-8711.1999.02853.x
6. Zhang, X., Lu, Y. and Liu, Z. (2019). Effect of Accreting Tidally Disrupted Stars on the Spin Evolution of $\sim 10^6\ M_\odot$ Black Holes. *Astrophys. J.* **877**:143. DOI:10.3847/1538-4357/ab1d48
7. Zubovas, K. (2019). Tidal disruption events can power the observed AGN in dwarf galaxies. *Mon. Not. R. Astron. Soc.* **483**:1957–1969. DOI:10.1093/mnras/sty3211
8. Ferrarese, L. and Ford, H. (2005). Supermassive Black Holes in Galactic Nuclei: Past, Present and Future Research. *Space Sci. Rev.* **116**:523–624. DOI:10.1007/s11214-005-3947-6
9. Netzer, H. (2015). Revisiting the Unified Model of Active Galactic Nuclei. *Annu. Rev. Astron. Astrophys.* **53**:365–408. DOI:10.1146/annurev-astro-082214-122302
10. Rees, M.J. (1988). Tidal disruption of stars by black holes of 10^6-10^8 solar masses in nearby galaxies. *Nature* **333**:523–528. DOI:10.1038/333523a0
11. Komossa, S. and Bade, N. (1999). The giant X-ray outbursts in NGC 5905 and IC 3599: Follow-up observations and outburst scenarios. *Astron. Astrophys.* **343**:775–787. DOI:10.48550/arXiv.astro-ph/9901141
12. Sazonov, S., Gilfanov, M., Medvedev, P. et al. (2021). First tidal disruption events discovered by SRG/eROSITA: X-ray/optical properties and X-ray luminosity function at z < 0.6. *Mon. Not. Roy. Astron. Soc.* **508**:3820–3847. DOI:10.1093/mnras/stab2843
13. Hammerstein, E., van Velzen, S., Gezari, S. et al. (2023). The Final Season Reimagined: 30 Tidal Disruption Events from the ZTF-I Survey. *Astrophys. J.* **942**:9. DOI:10.3847/1538-4357/aca283
14. Guillochon, J. and Ramirez-Ruiz, E. (2013). Hydrodynamical Simulations to Determine the Feeding Rate of Black Holes by the Tidal Disruption of Stars: The Importance of the Impact Parameter and Stellar Structure. *Astrophys. J.* **767**:25. DOI:10.1088/0004-637X/767/1/25
15. Coughlin, E.R. and Nixon, C.J. (2019). Partial Stellar Disruption by a Supermassive Black Hole: Is the Light Curve Really Proportional to $t^{-9/4}$? *Astrophys. J. Lett.* **883**:L17. DOI:10.3847/2041-8213/ab412d
16. Phinney, E.S. (1989). Manifestations of a Massive Black Hole in the Galactic Center. In The Center of the Galaxy, *136*, M. Morris, ed., p. 543
17. Ryu, T., Krolik, J., Piran, T. et al. (2020). Tidal Disruptions of Main-sequence Stars. III. Stellar Mass Dependence of the Character of Partial Disruptions. *Astrophys. J.* **904**:100. DOI:10.3847/1538-4357/abb3ce
18. Burrows, D.N., Kennea, J.A., Ghisellini, G. et al. (2011). Relativistic jet activity from the tidal disruption of a star by a massive black hole. *Nature* **476**:421–424. DOI:10.1038/nature10374
19. Liu, F.K., Li, S. and Chen, X. (2009). Interruption of Tidal-Disruption Flares by Supermassive Black Hole Binaries. *Astrophys. J.* **706**:L133–L137. DOI:10.1088/0004-637X/706/1/L133
20. Liu, F.K., Li, S. and Komossa, S. (2014). A Milliparsec Supermassive Black Hole Binary Candidate in the Galaxy SDSS J120136.02+300305.5. *Astrophys. J.* **786**:103. DOI:10.1088/0004-637X/786/2/103
21. Shu, X., Zhang, W., Li, S. et al. (2020). X-ray flares from the stellar tidal disruption by a candidate supermassive black hole binary. *Nat. Commun.* **11**:5876. DOI:10.1038/s41467-020-19675-z
22. Saxton, R., Komossa, S., Auchettl, K. et al. (2020). X-Ray Properties of TDEs. *Space Sci. Rev.* **216**:85. DOI:10.1007/s11214-020-00708-4
23. Andreoni, I., Coughlin, M.W., Perley, D.A. et al. (2022). A very luminous jet from the disruption of a star by a massive black hole. *Nature* **612**:430–434. DOI:10.1038/s41586-022-05465-8
24. Luo, B., Brandt, W.N., Xue, Y.Q. et al. (2017). The Chandra Deep Field-South Survey: 7 Ms Source Catalogs. *Astrophys. J., Suppl. Ser.* **228**:2. DOI:10.3847/1538-4365/228/1/2
25. Xue, Y.Q. (2017). The Chandra deep fields: Lifting the veil on distant active galactic nuclei and X-ray emitting galaxies. *New Astron. Rev.* **79**:59–84. DOI:10.1016/j.newar.2017.09.002
26. Lehmer, B.D., Brandt, W.N., Alexander, D.M. et al. (2005). The Extended Chandra Deep Field-South Survey: Chandra Point-Source Catalogs. *Astrophys. J., Suppl. Ser.* **161**:21–40. DOI:10.1086/444590
27. Xue, Y.Q., Luo, B., Brandt, W.N. et al. (2016). The 2 Ms Chandra Deep Field-North Survey and the 250 ks Extended Chandra Deep Field-South Survey: Improved Point-source Catalogs. *Astrophys. J., Suppl. Ser.* **224**:15. DOI:10.3847/0067-0049/224/2/15
28. Ranalli, P., Comastri, A., Vignali, C. et al. (2013). The XMM deep survey in the CDF-S. III. Point source catalogue and number counts in the hard X-rays. *Astron. Astrophys.* **555**:A42. DOI:10.1051/0004-6361/201321211
29. Ni, Q., Brandt, W.N., Chen, C.-T. et al. (2021). The XMM-SERVS Survey: XMM-Newton Point-source Catalogs for the W-CDF-S and ELAIS-S1 Fields. *Astrophys. J., Suppl. Ser.* **256**:21. DOI:10.3847/1538-4365/ac0dc6
30. Truemper, J. (1982). The ROSAT mission. *Adv. Space Res.* **2**:241–249. DOI:10.1016/0273-1177(82)90070-9
31. Burrows, D.N., Hill, J.E., Nousek, J.A. et al. (2005). The Swift X-Ray Telescope. *Space Sci. Rev.* **120**:165–195. DOI:10.1007/s11214-005-5097-2
32. Merloni, A., Lamer, G., Liu, T. et al. (2024). The SRG/eROSITA all-sky survey. First X-ray catalogues and data release of the western Galactic hemisphere. *Astron. Astrophys.* **682**:A34. DOI:10.1051/0004-6361/202347165
33. Cousins, R.D., Linnemann, J.T. and Tucker, J. (2008). Evaluation of three methods for calculating statistical significance when incorporating a systematic uncertainty into a test of the background-only hypothesis for a Poisson process. *Nucl. Instrum. Methods Phys. Res.* **595**:480–501. DOI:10.1016/j.nima.2008.07.086
34. Stark, A.A., Gammie, C.F., Wilson, R.W. et al. (1992). The Bell Laboratories H i Survey. *Astrophys. J., Suppl. Ser.* **79**:77. DOI:10.1086/191645
35. Vianello, G. (2018). Bias in profile poisson likelihood. GitHub. https://giacomov.github.io/Bias-in-profile-poisson-likelihood/
36. Bradley, L., Sipőcz, B., Robitaille, T. et al. (2023). astropy/photutils: 1.8.0. zenodo
37. Yang, G., Boquien, M., Brandt, W.N. et al. (2022). Fitting AGN/Galaxy X-Ray-to-radio SEDs with CIGALE and Improvement of the Code. *Astrophys. J.* **927**:192. DOI:10.3847/1538-4357/ac4971
38. Damen, M., Labbé, I., van Dokkum, P.G. et al. (2011). The SIMPLE Survey: Observations, Reduction, and Catalog. *Astrophys. J.* **727**:1. DOI:10.1088/0004-637X/727/1/1
39. Elbaz, D., Dickinson, M., Hwang, H.S. et al. (2011). GOODS-Herschel: an infrared main sequence for star-forming galaxies. *Astron. Astrophys.* **533**:A119. DOI:10.1051/0004-6361/201117239
40. Magnelli, B., Elbaz, D., Chary, R.R. et al. (2011). Evolution of the dusty infrared luminosity function from z = 0 to z = 2.3 using observations from Spitzer. *Astron. Astrophys.* **528**:A35. DOI:10.1051/0004-6361/200913941
41. Barger, A.J., Cowie, L.L., Bauer, F.E. et al. (2019). A Submillimeter Perspective on the GOODS Fields (SUPER GOODS). IV. The Submillimeter Properties of X-Ray Sources in the CDF-S. *Astrophys. J.* **887**:23. DOI:10.3847/1538-4357/ab5116
42. Peng, C.Y., Ho, L.C., Impey, C.D. et al. (2002). Detailed Structural Decomposition of Galaxy Images. *Astron. Now.* **124**:266–293. DOI:10.1086/340952
43. Oke, J.B., Cohen, J.G., Carr, M. et al. (1995). The Keck Low-Resolution Imaging Spectrometer. *Publ. Astron. Soc. Pac.* **107**:375. DOI:10.1086/133562
44. Perley, D.A. (2019). Fully Automated Reduction of Longslit Spectroscopy with the Low Resolution Imaging Spectrometer at the Keck Observatory. *Publ. Astron. Soc. Pac.* **131**:084503. DOI:10.1088/1538-3873/ab215d
45. Schlafly, E.F. and Finkbeiner, D.P. (2011). Measuring Reddening with Sloan Digital Sky Survey Stellar Spectra and Recalibrating SFD. *Astrophys. J.* **737**:103. DOI:10.1088/0004-637X/737/2/103
46. Fitzpatrick, E.L. (1999). Correcting for the Effects of Interstellar Extinction. *Publ. Astron. Soc. Pac.* **111**:63–75. DOI:10.1086/316293
47. Cappellari, M. and Emsellem, E. (2004). Parametric Recovery of Line-of-Sight Velocity Distributions from Absorption-Line Spectra of Galaxies via Penalized Likelihood. *Publ. Astron. Soc. Pac.* **116**:138–147. DOI:10.1086/381875
48. Cappellari, M. (2017). Improving the full spectrum fitting method: accurate convolution with Gauss-Hermite functions. *Mon. Not. R. Astron. Soc.* **466**:798–811. DOI:10.1093/mnras/stw3020
49. Balestra, I., Mainieri, V., Popesso, P. et al. (2010). The Great Observatories Origins Deep Survey. VLT/VIMOS spectroscopy in the GOODS-south field: Part II. *Astron. Astrophys.* **512**:A12. DOI:10.1051/0004-6361/200913626
50. Szokoly, G.P., Bergeron, J., Hasinger, G. et al. (2004). The Chandra Deep Field-South: Optical Spectroscopy. I. *Astrophys. J., Suppl. Ser.* **155**:271–349. DOI:10.1086/424707
51. Avni, Y. (1976). Energy spectra of X-ray clusters of galaxies. *Astrophys. J.* **210**:642–646. DOI:10.1086/154870
52. Vanden Berk, D.E., Richards, G.T., Bauer, A. et al. (2001). Composite Quasar Spectra from the Sloan Digital Sky Survey. *Astron. Now.* **122**:549–564. DOI:10.1086/321167
53. Evans, C.R. and Kochanek, C.S. (1989). The Tidal Disruption of a Star by a Massive Black Hole. *Astrophys. J. Lett.* **346**:L13. DOI:10.1086/185567
54. Giacconi, R., Zirm, A., Wang, J. et al. (2002). Chandra Deep Field South: The 1 Ms Catalog. *Astrophys. J., Suppl. Ser.* **139**:369–410. DOI:10.1086/338927
55. Zheng, X.C., Xue, Y.Q., Brandt, W.N. et al. (2017). Deepest View of AGN X-Ray Variability with the 7 Ms Chandra Deep Field-South Survey. *Astrophys. J.* **849**:127. DOI:10.3847/1538-4357/aa9378
56. Bauer, F.E., Treister, E., Schawinski, K. et al. (2017). A new, faint population of X-ray transients. *Mon. Not. R. Astron. Soc.* **467**:4841–4857. DOI:10.1093/mnras/stx417
57. Xue, Y.Q., Zheng, X.C., Li, Y. et al. (2019). A magnetar-powered X-ray transient as the aftermath of a binary neutron-star merger. *Nature* **568**:198–201. DOI:10.1038/s41586-019-1079-5
58. Yu, L.-M., Luo, B., Brandt, W.N. et al. (2023). X-Ray Unveiling Events in a z ≈ 1.6 Active Galactic Nucleus in the 7 Ms Chandra Deep Field-South. *Astrophys. J.* **949**:6. DOI:10.3847/1538-4357/acc17e
59. Franzen, T.M.O., Sadler, E.M., Chhetri, R. et al. (2014). Deep 20-GHz survey of the Chandra Deep Field South and SDSS Stripe 82: source catalogue and spectral properties. *Mon. Not. R. Astron. Soc.* **439**:1212–1230. DOI:10.1093/mnras/stt2322
60. Huynh, M.T., Hopkins, A.M., Lenc, E. et al. (2012). The ATLAS 5.5 GHz survey of the extended Chandra Deep Field South: catalogue, source counts and spectral indices. *Mon. Not. R. Astron. Soc.* **426**:2342–2358. DOI:10.1111/j.1365-2966.2012.21894.x
61. Zinn, P.C., Middelberg, E., Norris, R.P. et al. (2012). The Australia Telescope Large Area Survey: 2.3 GHz observations of ELAIS-S1 and CDF-S. Spectral index properties of the faint radio sky. *Astron. Astrophys.* **544**:A38. DOI:10.1051/0004-6361/201219349
62. Miller, N.A., Fomalont, E.B., Kellermann, K.I. et al. (2008). The VLA 1.4 GHz Survey of the Extended Chandra Deep Field-South: First Data Release. *Astrophys. J., Suppl. Ser.* **179**:114–123. DOI:10.1086/591054
63. Miller, N.A., Bonzini, M., Fomalont, E.B. et al. (2013). The Very Large Array 1.4 GHz Survey of the Extended Chandra Deep Field South: Second Data Release. *Astrophys. J., Suppl. Ser.* **205**:13. DOI:10.1088/0067-0049/205/2/13
64. Norris, R.P., Afonso, J., Appleton, P.N. et al. (2006). Deep ATLAS Radio Observations of the Chandra Deep Field-South/Spitzer Wide-Area Infrared Extragalactic Field. *Astron. Now.* **132**:2409–2423. DOI:10.1086/508275

65. Hales, C.A., Norris, R.P., Gaensler, B.M. et al. (2014). ATLAS 1.4 GHz data release 2 - II. Properties of the faint polarized sky. *Mon. Not. R. Astron. Soc.* **440**:3113–3139. DOI:10.1093/mnras/stu500
66. Condon, J.J., Cotton, W.D., Greisen, E.W. et al. (1998). The NRAO VLA Sky. *Survey Astron* **J115**:1693–1716. DOI:10.1086/300337
67. Afonso, J., Messias, H., Mobasher, B. et al. (2007). Deep ATCA and GMRT Observations of the CDFS. In Deepest Astronomical Surveys, Vol. 380 of Astronomical Society of the Pacific Conference Series, J. Afonso, H.C. Ferguson, and B. Mobasher et al., eds., p. 243
68. Wayth, R.B., Lenc, E., Bell, M.E. et al. (2015). GLEAM: The GaLactic and Extragalactic All-Sky MWA Survey. *Publ. Astron. Soc. Aust.* **32**:e025. DOI:10.1017/pasa.2015.26
69. Hurley-Walker, N., Morgan, J., Wayth, R.B. et al. (2014). The Murchison Widefield Array Commissioning Survey: A Low-Frequency Catalogue of 14 110 Compact Radio Sources over 6 100 Square Degrees. *Publ. Astron. Soc. Aust.* **31**:e045. DOI:10.1017/pasa.2014.40
70. Cohen, A.S., Lane, W.M., Cotton, W.D. et al. (2007). The VLA Low-Frequency Sky. *Survey Astron* **J134**:1245–1262. DOI:10.1086/520719
71. Kellermann, K.I., Fomalont, E.B., Mainieri, V. et al. (2008). The VLA Survey of the Chandra Deep Field-South. I. Overview and the Radio Data. *Astrophys. J., Suppl. Ser.* **179**:71–94. DOI:10.1086/591055
72. Gim, H.B., Yun, M.S., Owen, F.N. et al. (2019). Nature of Faint Radio Sources in GOODS-North and GOODS-South Fields. I. Spectral Index and Radio-FIR Correlation. *Astrophys. J.* **875**:80. DOI:10.3847/1538-4357/ab1011
73. Alberts, S., Rujopakarn, W., Rieke, G.H. et al. (2020). Completing the Census of AGN in GOODS-S/HUDF: New Ultradeep Radio Imaging and Predictions for JWST. *Astrophys. J.* **901**:168. DOI:10.3847/1538-4357/abb1a0
74. Lacy, M., Baum, S.A., Chandler, C.J. et al. (2020). The Karl G. Jansky Very Large Array Sky Survey (VLASS). Science Case and Survey Design. *Publ. Astron. Soc. Pac.* **132**:035001. DOI:10.1088/1538-3873/ab63eb
75. Trump, J.R., Impey, C.D., Taniguchi, Y. et al. (2009). The Nature of Optically Dull Active Galactic Nuclei in COSMOS. *Astrophys. J.* **706**:797–809. DOI:10.1088/0004-637X/706/1/797
76. Lehmer, B.D., Basu-Zych, A.R., Mineo, S. et al. (2016). The Evolution of Normal Galaxy X-Ray Emission through Cosmic History: Constraints from the 6 MS Chandra Deep Field-South. *Astrophys. J.* **825**:7. DOI:10.3847/0004-637X/825/1/7
77. Farrell, S.A., Webb, N.A., Barret, D. et al. (2009). An intermediate-mass black hole of over 500 solar masses in the galaxy ESO243-49. *Nature* **460**:73–75. DOI:10.1038/nature08083
78. Bosch, R.C.E.v.d. (2016). Unification of the fundamental plane and Super Massive Black Hole Masses. *Astrophys. J.* **831**:134. DOI:10.3847/0004-637X/831/2/134
79. Gezari, S. (2021). Tidal Disruption Events. *Annu. Rev. Astron. Astrophys.* **59**:21–58. DOI:10.1146/annurev-astro-111720-030029
80. Timlin, J.D., III, Brandt, W.N., Zhu, S. et al. (2020). The frequency of extreme X-ray variability for radio-quiet quasars. *Mon. Not. R. Astron. Soc.* **498**:4033–4050. DOI:10.1093/mnras/staa2661
81. Dai, L., McKinney, J.C. and Miller, M.C. (2015). Soft x-ray temperature tidal disruption events from stars on deep plunging orbits. *ApJL* **812**:L39. DOI:10.1088/2041-8205/812/2/l39
82. Bonnerot, C., Rossi, E.M. and Lodato, G. (2017). Long-term stream evolution in tidal disruption events. *MNRAS* **464**:2816–2830. DOI:10.1093/mnras/stw2547
83. Chen, J.-H. and Shen, R.-F. (2021). Light Curves of Partial Tidal Disruption Events. *Astrophys. J.* **914**:69. DOI:10.3847/1538-4357/abf9a7
84. Bonnerot, C., Lu, W. and Hopkins, P.F. (2021). First light from tidal disruption events. *MNRAS* **504**:4885–4905. DOI:10.1093/mnras/stab398
85. Yuan, W., Zhang, C., Chen, Y. et al. (2018). Einstein Probe: Exploring the ever-changing X-ray Universe. *Sci. Sin. -Phys. Mech. Astron.* **48**:039502. DOI:10.1360/SSPMA2017-00297
86. Jin, C.C., Li, D.Y., Jiang, N. et al. (2025). An Intermediate-mass Black Hole Lurking in A Galactic Halo Caught Alive during Outburst. Preprint at *arXiv*. DOI:10.48550/arXiv.2501.09580